

Prospects of constraining on the polarizations of gravitational waves from binary black holes using space- and ground-based detectors

Jie Wu (吴洁)[✉] and Jin Li (李瑾)[✉]

*College of Physics, Chongqing University, Chongqing 401331, China and
Department of Physics and Chongqing Key Laboratory for Strongly Coupled Physics,
Chongqing University, Chongqing 401331, China*

In general relativity, gravitational waves (GWs) exhibit two tensor modes, while alternative theories predict up to six polarization modes. We investigate GW polarization constraints using a model-independent parametrized post-Einsteinian framework with space- and ground-based detectors. Evaluating LISA, Taiji, TianQin, LIGO, Virgo, KAGRA, and Einstein Telescope (ET), we analyze their capabilities and network performance. Taiji provides the best constraints among space-based detectors, with LISA outperforming TianQin. Among ground-based detectors, LIGO excels in vector modes, while ET offers the most comprehensive constraints. In network scenarios, LISA+TJm performs best, and ET surpasses second-generation detector combinations. Multiband observations alleviate scalar mode degeneracies, significantly enhancing ground-based detector performance. Combined space- and ground-based observations yield robust constraints on GW polarization, advancing tests of deviations from general relativity. Our findings highlight the potential of future GW missions to refine our understanding of gravitational physics through precise polarization measurements.

I. INTRODUCTION

Over the past century, general relativity (GR) has been rigorously tested through numerous solar system experiments and astrophysical observations, with no definitive evidence suggesting deviations from GR [1–3]. Despite passing all experimental tests, there are indications that GR may need to be extended, particularly due to the challenges posed by dark energy and dark matter in cosmology [4, 5]. Gravitational waves (GWs) offer a new avenue for testing GR, especially in the strong-field regime where GWs are generated by compact objects [6]. One method to test GR is by detecting additional polarizations of GWs. In GR, GWs only have two tensor modes, whereas some alternative gravity theories predict up to six polarization modes [7]. For instance, Brans-Dicke theory predicts an additional scalar mode [2, 8], while $f(R)$ theory and Horndeski theory propose two additional scalar modes [9–11]. Einstein-Aether theory predicts five polarization modes [12, 13], and some tensor-vector-scalar theories encompass all six polarization modes [14, 15]. Therefore, detecting additional polarizations of GWs can help identify deviations from GR, surpass current experimental limits, and reveal the deeper nature of gravity.

Since LIGO first detected GW [16], nearly a hundred GW events generated by compact binary coalescences (CBCs) have been observed [17–19]. Testing GR with these GW data has shown that all observed data are consistent with GR so far [20–26]. With the commencement of the fourth observation run (O4), more GW events are expected to be detected, allowing for further testing of GR. In general, to detect the polarization of transient

GWs, more detectors are needed to obtain responses from different directions, thereby enhancing detection capabilities [27]. Ground-based detectors in the hertz frequency band, such as LIGO [28], Virgo [29], and KAGRA [30], collaborate to form a detector network to detect the polarization of GWs. For continuous GWs emitted by distant CBCs, a detector with directional change capability is sufficient [27]. Space-based GW detectors in the millihertz frequency band, such as LISA [31], Taiji [32], and TianQin [33], consist of three spacecraft orbiting the Sun/Earth in a triangular formation, making it possible to detect additional GW polarizations due to the detector's motion in space [34].

Besides determining whether the detector can theoretically detect additional polarizations of GWs, it is also crucial to ascertain whether the detected GW signal is consistent with the predictions of GR. One approach is to use a waveform model with purely phenomenological parameters to represent possible deviations from GR and to apply constraints to these parameters using observed GW data [6]. Yunes and Pretorius proposed the parameterized post-Einstein (ppE) waveform [35], based on the post-Newtonian (PN) approximation, which is suitable for parameterizing the influence of alternative gravity theories on non-GR polarizations. Most modified gravity theories, such as Brans-Dicke theory, massive gravity, and bimetric theory, can be described using the ppE framework [36]. Although the ppE framework cannot parameterize all possible deviations from GR, it can test for additional polarizations, providing a method to evaluate the performance of detectors in testing GR [37–39].

Currently, some work utilizes the ppE framework to constrain additional polarizations for testing GR. Narikawa and Tagoshi discussed the potential of advanced ground-based GW detectors, such as LIGO, Virgo, and KAGRA, in detecting general deviations between GWs and the predictions of GR using the ppE

* cqujinli1983@cqu.edu.cn

framework [40]. Huwyler *et al.* employed LISA to detect massive black hole binaries (MBHBs) and test GR by representing ppE waveforms with phase corrections only [41]. References [6, 36] discussed the potential of Taiji and TianQin in using MBHBs to test GR and provide constraints on non-GR parameters. For detector networks, Nair *et al.* focused on the synergistic effect of the Einstein Telescope (ET) and preDECIGO, demonstrating enhanced sensitivity within a specific band [42]. In Ref. [43], Wang and Han used the LISA-Taiji network to test the ppE parameters of deviations from the GR waveform, indicating a significant improvement in the detection of polarization amplitude through joint observations.

Based on our previous work [44–46], we investigate the constraints from binary black holes (BBHs) for alternative configurations of space- and ground-based detectors on the detection of additional GW polarizations. We employ the ppE framework for model-independent testing in GR by numerically calculating time-domain GW signals that contain all polarizations. Space-based detectors LISA, Taiji, and TianQin are used to observe massive black hole binaries (MBHBs), while ground-based detectors LIGO, Virgo, KAGRA, and the Einstein Telescope (ET) observe stellar-mass binary black holes (SBBHs), providing constraint results under different networks. We also consider the combination of multiband observations. The long-term observation of SBBHs by space-based detectors helps break the response degeneracy of ground-based detectors, thereby improving constraints. Using the Fisher information matrix (FIM), we present the constraint results of several typical mass BBHs as a function of redshift. Additionally, we discuss the potential effects of multimessenger observations on enhancing parameter constraints. Through systematic research, we comprehensively analyze the results of additional GW polarizations constrained by space- and ground-based detectors from multiple perspectives.

This paper is organized as follows. In Sec. II, we introduce time-domain GW signals and ppE parameters for measuring additional polarizations within the ppE framework. In Sec. III, we review the performance parameters and alternative configurations of space- and ground-based detectors, and analyze the response functions corresponding to different modes. In Sec. IV, we explain the typical BBH sources selected in our paper and the method for calculating the signal-to-noise ratio (SNR) and FIM. In Sec. V, we present the constraint results on ppE parameters, including observations from different networks, multiband, and multimessenger observations. Finally, we summarize the results of our research in Sec. VI.

II. GRAVITATIONAL WAVE SIGNAL

In generalized modified gravity theories, metric perturbations can have up to six independent degrees of free-

dom, resulting in six different polarization modes: two tensor modes (+ and \times), two vector modes (X and Y) and two scalar modes (B and L) [47]. For detectors, the observed GW strain can be described as a linear combination of different GW polarizations, expressed as

$$h(t) = \sum_A F^A h_A(t), \quad (1)$$

where $A = \{+, \times, X, Y, B, L\}$ represents for the six polarizations, $h_A(t)$ is the input signal of GWs, and F^A is the angular response function.

The extended ppE framework is used to construct a model-independent test for GR, including all GW polarization modes [37]. The amplitude and phase of GWs can be obtained separately from the measurement of perturbations and energy evolution, and there exist simultaneous quadrupole and dipole radiation. The process of CBC includes three phases: inspiral, merger, and ring-down. Currently, the observed GW events are transient and do not include the early inspiral phase [19]. Moreover, GR has passed all current experimental tests, indicating that only tensor modes generated by quadrupole radiation are present in the non-inspiral phase. The contribution of dipole radiation in the early inspiral phase can be greater than during the merger phase [36, 48]. Therefore, it is reasonable to assume that tensor modes dominate in quadrupole radiation, while vector and scalar modes dominate in dipole radiation. Following Refs. [36, 37, 47, 49], the GW waveform under the ppE framework can be written as

$$\begin{aligned} h_+ &= \mathcal{A}_T (1 + \cos^2 \iota) / 2 \cos(2\Phi + 2\Phi_0), \\ h_\times &= \mathcal{A}_T \cos \iota \sin(2\Phi + 2\Phi_0), \\ h_X &= \mathcal{A}_V \cos \iota \cos(\Phi + \Phi_0), \\ h_Y &= \mathcal{A}_V \sin(\Phi + \Phi_0), \\ h_B &= \mathcal{A}_B \sin \iota \cos(\Phi + \Phi_0), \\ h_L &= \mathcal{A}_L \sin \iota \cos(\Phi + \Phi_0), \end{aligned} \quad (2)$$

with

$$\begin{aligned} \mathcal{A}_T &= \frac{4}{D_L} \left(\frac{G\mathcal{M}}{c^2} \right)^{5/3} \left(\frac{\omega}{c} \right)^{2/3}, \\ \mathcal{A}_V &= \frac{\alpha_V}{D_L} \left(\frac{G\mathcal{M}}{c^2} \right)^{4/3} \left(\frac{\omega}{c} \right)^{1/3}, \\ \mathcal{A}_B &= \frac{\alpha_B}{D_L} \left(\frac{G\mathcal{M}}{c^2} \right)^{4/3} \left(\frac{\omega}{c} \right)^{1/3}, \\ \mathcal{A}_L &= \frac{\alpha_L}{D_L} \left(\frac{G\mathcal{M}}{c^2} \right)^{4/3} \left(\frac{\omega}{c} \right)^{1/3}, \end{aligned} \quad (3)$$

where $\alpha_{V,B,L}$ are the dimensionless ppE parameters, $\mathcal{M} = (m_1 m_2)^{3/5} / (m_1 + m_2)^{1/5}$ is the chirp mass, m_1 and m_2 are the masses of BBH, D_L is the luminosity distance, ι is the inclination angle, $\Phi = \int \omega dt$ is the orbital phase, ω is the orbital angular frequency, Φ_0 is the initial orbital phase, G and c are the gravitational constant and the speed of light.

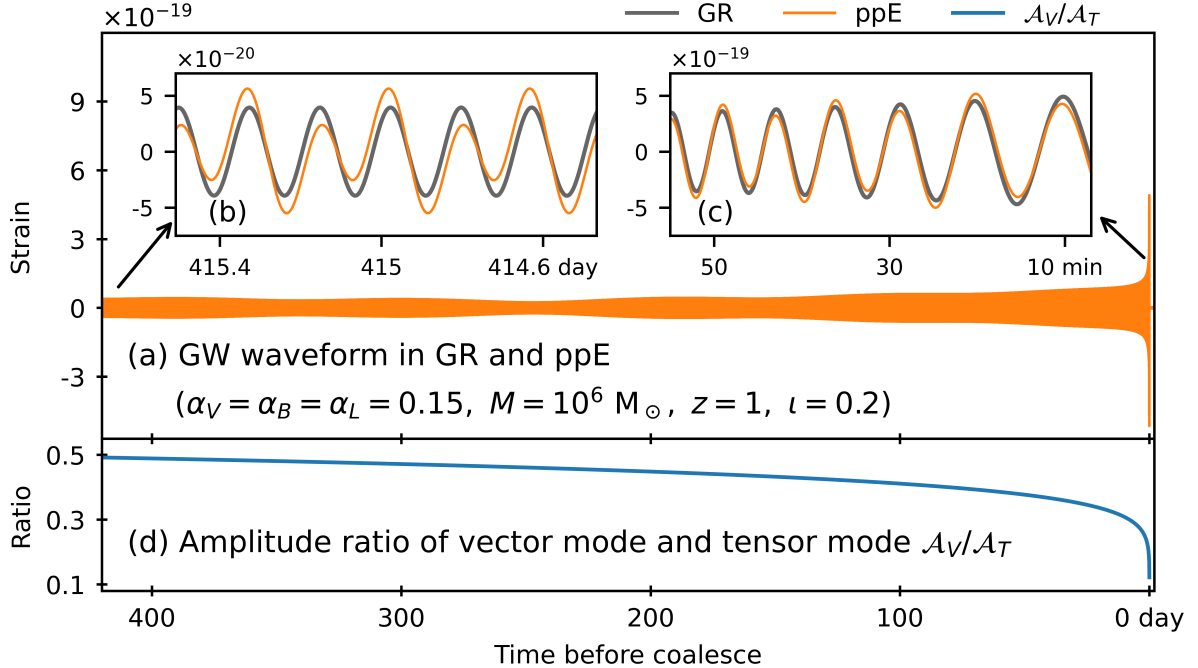


FIG. 1. Comparison of time-domain GW waveforms under GR and ppE frameworks. The GW waveform of an MBHB with a total mass of $10^5 M_\odot$ is observed by LISA over the year before coalescence. To clearly visualize differences, we set $\alpha_D = 0.001$, $\alpha_Q = 96/5$, and $\alpha_V = \alpha_B = \alpha_L = 0.15$, ensuring $A_V = A_B = A_L$. (a) displays the specific time-domain GW signal. (b) and (c) show the GW waveforms from 415 days and 30 minutes before coalescence, reflecting the early and late inspiral phases, respectively. (d) illustrates the ratio of the amplitude of additional modes to the tensor modes.

We only consider the dominant modes in different radiations for the amplitude, and the contribution of different radiations to the orbital angular frequency varies. Considering the influence of possible non-dominant modes, the overall evolution of the orbital angular frequency can be described by the contributions of dipole radiation and quadrupole radiation [36, 49]:

$$\frac{d\omega}{dt} = \alpha_D \eta^{2/5} \frac{GM}{c^3} \omega^3 + \alpha_Q \left(\frac{GM}{c^3} \right)^{5/3} \omega^{11/3}, \quad (4)$$

where α_D and α_Q are the ppE parameters that describe the orbital angular frequency contributions of dipole and quadrupole radiation, $\eta = m_1 m_2 / M^2$ is the symmetric mass ratio, and $M = m_1 + m_2$ is the total mass.

To describe the model-independent GW waveform, we select five dimensionless ppE parameters to constrain parameters in alternative gravity theories. In the case of GR, $\alpha_{D,V,B,L} = 0$ and $\alpha_Q = 96/5$. To ensure our analysis remains independent of specific models, we treat these ppE parameters as independent. Some theories exhibit correlations between these parameters, potentially enhancing parameter constraints [36]. Thus, our results are conservative, and the actual constraints may exceed those presented here.

From Eq. (4), solving the evolution function $\omega(t)$ of the orbital angular frequency over time analytically is

challenging. We determine $t(\omega)$ through integration::

$$t = t_0 + \int_{\omega(t_0)}^{\omega(t)} \left(\frac{d\omega}{dt} \right)^{-1} d\omega, \quad (5)$$

which is shown in Refs. [36, 49]. Computational methods, such as the bisection method, iteratively solve for the orbital angular frequency corresponding to a given time point. By solving point by point, we obtain $\omega(t)$. Using the above method, we input the calculated $\omega(t)$ into Eqs. (1)-(3) to derive the final GW signal.

In order to better demonstrate the impact of ppE parameters on GW waveforms significantly, we set large parameter values in Fig. 1. As shown in Fig. 1(b), there is a notable amplitude difference between the ppE waveform and the GR waveform. This discrepancy arises because the GW frequency from dipole radiation equals the orbital frequency of the BBH, whereas quadrupole radiation operates at twice that frequency. This effectively superimposes a waveform with half the frequency onto the original GR waveform, resulting in amplitude modulation at twice the wavelength. Comparing Figs. 1(b) and (c), the disparity between the ppE waveform and the GR waveform is significant when the merger is distant but diminishes as the merger approaches, consistent with our assumption in Eq. (2) to align with current GR testing outcomes. In Fig. 1(d), the ratio of additional

modes to tensor modes is visually depicted, showing a gradual decrease over time, causing the ppE waveform to progressively approach the GR waveform. From Eq. (3), it can be seen that the amplitude of the tensor modes varies with the power of $2/3$ of the angular frequency, while the additional modes varies with the power of $1/3$. The rate of amplitude increase for tensor modes is significantly greater than for additional modes, resulting in the ratio $\mathcal{A}_V/\mathcal{A}_T \propto \omega^{-1/3}$ declining as angular frequency increases.

III. DETECTORS AND RESPONSE

A. Space-based detectors

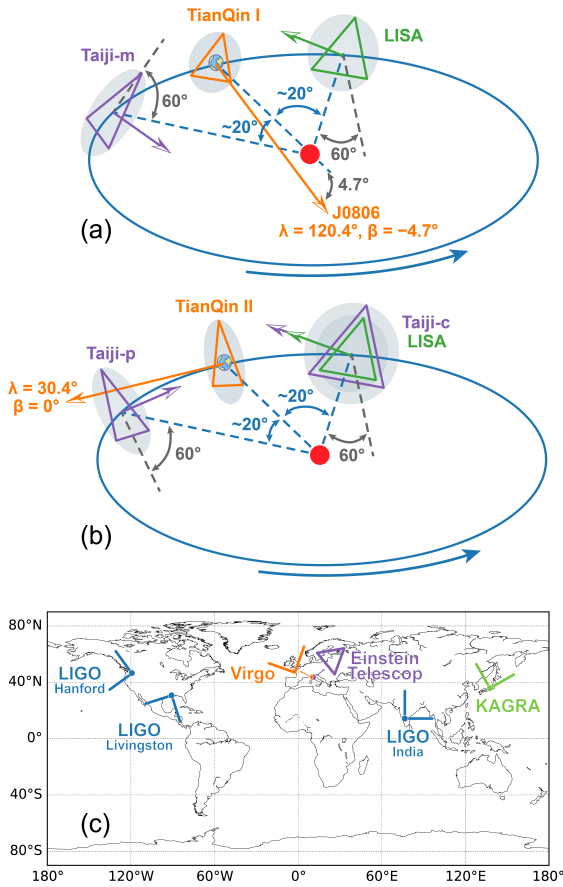


FIG. 2. Configuration and location of space- and ground-based detectors (not to scale). (a) and (b) depict alternative orbital configurations of LISA, Taiji-p, Taiji-c, Taiji-m, TianQin I, and TianQin II [44]. The solid arrow on the constellation plane represents the normal direction of the detector constellation plane. (c) shows the geographical locations and azimuth angles of LIGO, Virgo, KAGRA, and ET [50, 51].

In the 2030s, LISA, Taiji, and TianQin are scheduled to launch triangular constellations consisting of three spacecraft. LISA and Taiji utilize heliocentric orbits, whereas

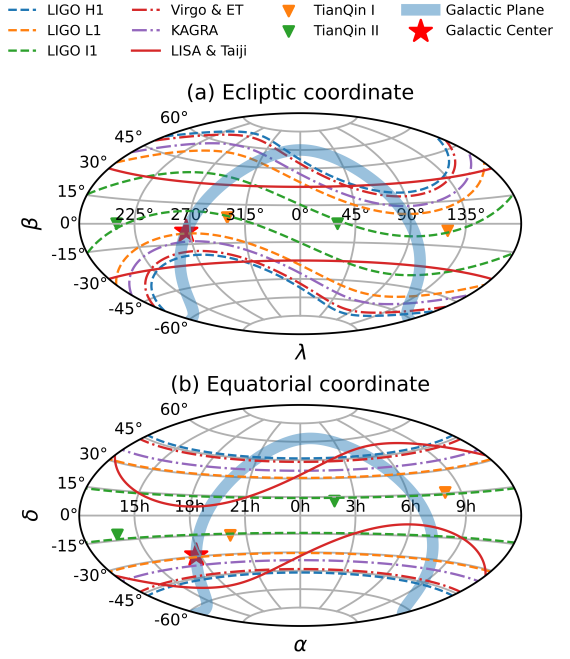


FIG. 3. The variation of the normal direction of the detector constellation plane during the observation period in the ecliptic (λ, β) and equatorial (α, δ) coordinate systems. This paper uses the obliquity of the ecliptic ($\varepsilon_{2000} = 23^\circ 26' 21''$) based on epoch J2000.0 for the conversion between these two coordinate systems [52].

TianQin employs geocentric orbits. Various alternative orbital configurations are available, as detailed in Figs. 2 and 3. LISA and Taiji, including three configurations, have a leading or trailing angle of 20° relative to Earth, with a 60° inclination between the constellation plane and the ecliptic plane [31, 32]. Furthermore, the normal direction of the TianQin constellation plane remains fixed, and TianQin follows a “three months on+three months off” observation scheme [33].

Variations in the constellation plane determine how GW sources appear in the detector coordinate system, thereby influencing the response to different polarizations. Additionally, detector sensitivity is directly influenced by the arm length, with LISA, Taiji, and TianQin having arm lengths of 2.5×10^6 km, 3×10^6 km, and $\sqrt{3} \times 10^5$ km, respectively. Concerning the noise in space-based detectors, we account for acceleration noise, displacement noise, and foreground noise. Acceleration noise and displacement noise contribute to the primary power spectral density (PSD), as detailed in Refs. [53–55]. Foreground noise originates from galactic binaries within the Milky Way galaxy, creating a peak in the frequency band of approximately 0.3–3 mHz, as demonstrated in our previous work [44].

B. Ground-based detectors

In contrast to the planned space-based detectors, the ground-based detectors are currently operational, primarily comprising the LVK collaboration, which includes LIGO, Virgo and KAGRA. These are all L-shaped second-generation detectors with arm lengths of 4 km (LIGO), 3 km (Virgo), and 3 km (KAGRA), respectively [28–30]. In this paper, we consider LIGO to include three detectors: LIGO Hanford (H1) and LIGO Livingston (L1), which are operational, and the planned LIGO India (I1). Furthermore, we consider the third-generation detector ET, which features a triangular shape composed of three 10 km arms [56].

As the Earth rotates, ground-based detectors scan different sky regions, as illustrated in Fig. 3. Due to the obliquity of the ecliptic, the sky regions scanned by space- and ground-based detectors is not parallel. Ground-based detectors, unlike their space-based counterparts, are affected by various types of noise, including quantum noise, seismic noise, gravity-gradient noise, thermal noise, and others. For our study, we utilize the design performance specifications of these detectors, and the corresponding PSD can be referenced in LIGO Document T1500293 and Refs. [57, 58].

C. Response function

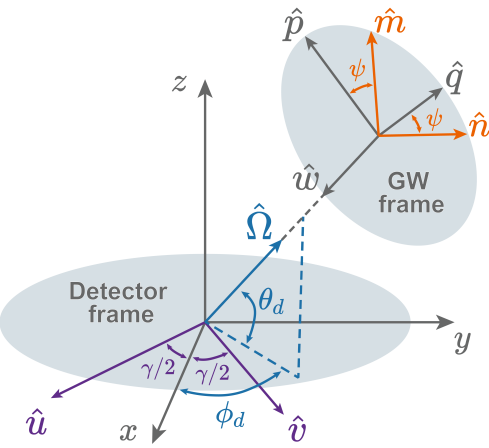


FIG. 4. Relationship between the detector coordinate and the GW coordinate [45].

A dual-arm Michelson interferometer detects GWs by measuring the relative change in the length of its two arms. We describe the detector's response to GWs using the method outlined in Refs. [27, 45]. As shown in Fig. 4, the detector coordinates are constructed using orthogonal unit vectors $\{\hat{x}, \hat{y}, \hat{z}\}$, and the GW coordinates are constructed using $\{\hat{p}, \hat{q}, \hat{w}\}$. Here, \hat{w} represents the propagation direction of the GW, and the unit vector $\hat{\Omega} = -\hat{w}$ represents the position of the GW source. In a triangular

detector, the angle γ between the two arms is 60° , while in an L-shaped detector, it is 90° . For GWs, an additional rotational degree of freedom can be fixed by specifying the polarization angle ψ , ultimately using $\{\hat{m}, \hat{n}, \hat{w}\}$ to describe the GW. The angular response function F^A in Eq. (1) can be expressed as

$$F^A = D^{ij} e_{ij}^A, \quad (6)$$

where the polarization tensor e_{ij}^A is described using the orthogonal unit vectors mentioned above [27, 59]:

$$\begin{aligned} e_{ij}^+ &= \hat{m}_i \hat{m}_j - \hat{n}_i \hat{n}_j, & e_{ij}^\times &= \hat{m}_i \hat{n}_j + \hat{n}_i \hat{m}_j, \\ e_{ij}^X &= \hat{m}_i \hat{w}_j + \hat{w}_i \hat{m}_j, & e_{ij}^Y &= \hat{n}_i \hat{w}_j + \hat{w}_i \hat{n}_j, \\ e_{ij}^B &= \hat{m}_i \hat{m}_j + \hat{n}_i \hat{n}_j, & e_{ij}^L &= \hat{w}_i \hat{w}_j. \end{aligned} \quad (7)$$

And the detector tensor D^{ij} can be written as [60]

$$D^{ij} = \frac{1}{2} [\hat{u}^i \hat{u}^j \mathcal{T}(f, \hat{u} \cdot \hat{w}) - \hat{v}^i \hat{v}^j \mathcal{T}(f, \hat{v} \cdot \hat{w})], \quad (8)$$

with

$$\begin{aligned} \mathcal{T}(f, \hat{a} \cdot \hat{b}) = & \frac{1}{2} \left\{ \sin c \left[\frac{f}{2f_*} (1 - \hat{a} \cdot \hat{b}) \right] \right. \\ & \times \exp \left[-i \frac{f}{2f_*} (3 + \hat{a} \cdot \hat{b}) \right] \\ & + \text{sinc} \left[\frac{f}{2f_*} (1 + \hat{a} \cdot \hat{b}) \right] \\ & \times \exp \left[-i \frac{f}{2f_*} (1 + \hat{a} \cdot \hat{b}) \right] \Big\}, \end{aligned} \quad (9)$$

where $\text{sinc}(x) = \sin x / x$, $f_* = c/(2\pi L)$ is the transfer frequency and L is the arm length of the detector. The transfer frequencies for space-based detectors are 19 mHz for LISA, 16 mHz for Taiji, and 275 mHz for TianQin. Due to the arm length, the transfer frequency of ground-based detectors is significantly higher than their sensitivity frequency band.

The angular response functions $F^A(\lambda, \beta, \psi)$ or $F^A(\alpha, \delta, \psi)$ are obtained by substituting the detector and ecliptic/equatorial coordinates into Eqs. (6)-(9) using Euler rotation conversion. To present the angular response function concisely, we introduce the combined tensor and vector modes:

$$\begin{aligned} F^T &= \sqrt{|F^+|^2 + |F^\times|^2}, \\ F^V &= \sqrt{|F^X|^2 + |F^Y|^2}. \end{aligned} \quad (10)$$

According to Ref. [27], the angular response functions of combined tensor mode F^T , combined vector mode F^V , breathing mode F^B , and longitudinal mode F^L are independent of the polarization angle ψ . In this section, we study the response of different modes using these four independent modes of ψ and the six basic modes for subsequent research and calculations. On this basis, we

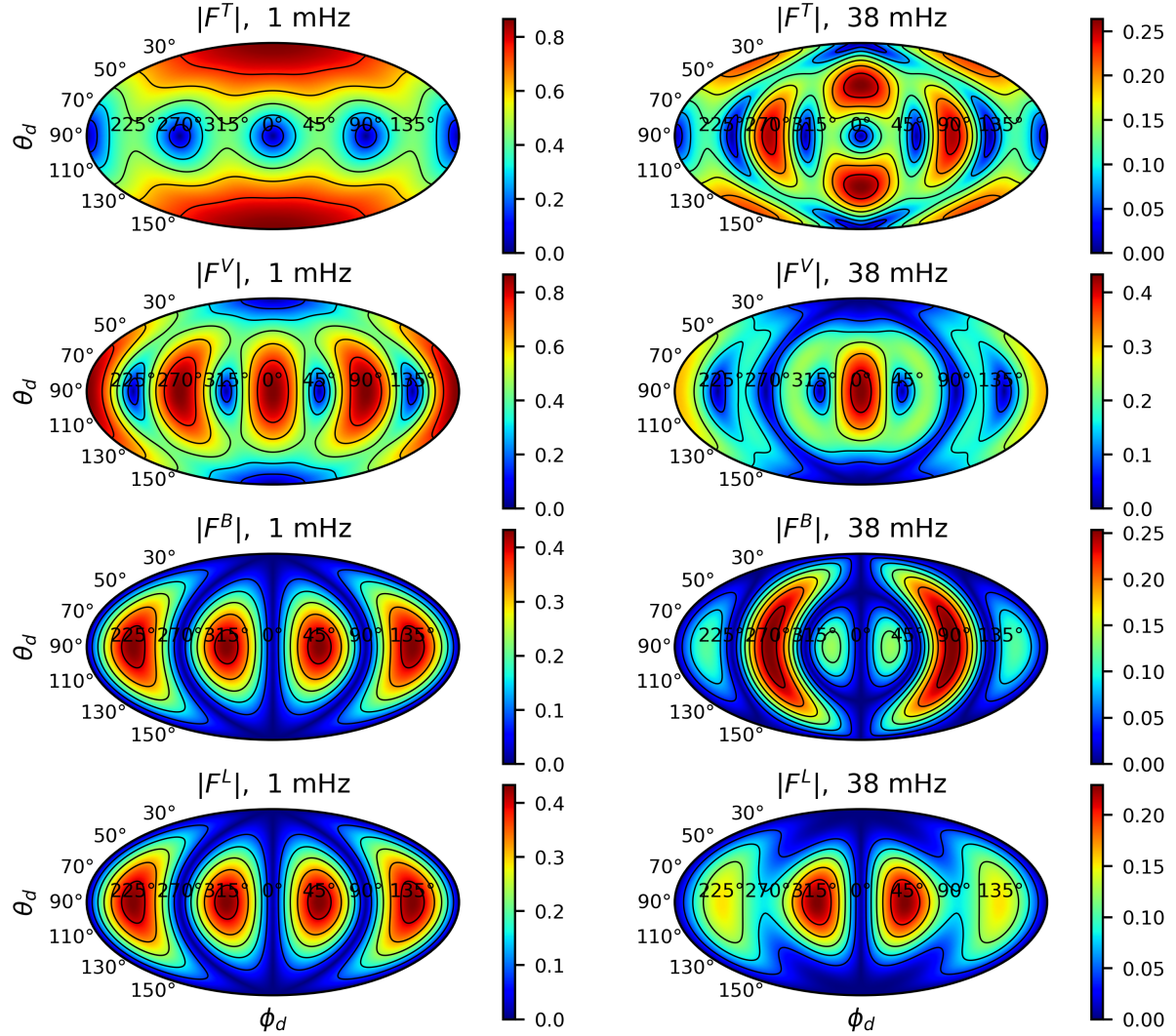


FIG. 5. Angular response functions for the combined tensor mode F^T , combined vector mode F^V , breathing mode F^B , and longitudinal mode F^L at LISA detector coordinates (ϕ_d, θ_d) . The left panel shows the response functions for GWs at 1 mHz, where the breathing and longitudinal modes are almost identical. The right panel displays the response at twice the transfer frequency, $2f_* = 38$ mHz, where the degeneracy between the breathing and longitudinal modes is broken at higher frequencies.

calculate the angular response functions for two different frequencies in the LISA detector coordinates to plot Fig. 5.

According to Eq. (9), at the low-frequency limit $f \ll f_*$, $\mathcal{T} \rightarrow 1$ leads to $F^B = -F^L$ [27]. Ground-based detectors operate within sensitivity frequency bands below the low-frequency limit, making it impossible to distinguish between these two modes. Moreover, space-based detectors may break through the low-frequency limit and resolve this degeneracy. Figure 5 shows that at the low-frequency limit, the angular response functions for the breathing mode and longitudinal mode are degenerate at every position. Beyond the transfer frequency, the optimal response position of the breathing mode shifts from $\phi_d = 45^\circ, 135^\circ, 225^\circ, 315^\circ$ to $\phi_d = 90^\circ, 270^\circ$. This shift, which differs from the longitudinal mode's optimal

response position, makes it possible to break the degeneracy of these two modes.

As shown in Fig. 5, the optimal response positions of the combined tensor mode and the combined vector mode change with frequency. The optimal position for the combined tensor mode shifts from a direction perpendicular to the constellation plane to a direction closer to it. For the combined vector mode, the optimal positions at $\phi_d = 90^\circ$ and $\phi_d = 270^\circ$ disappear as frequency increases. In summary, at frequencies beyond the low-frequency limit, there is no degeneracy among the modes, and the optimal response positions generally are not overlapped.

Figure 5 illustrates the response at two specific frequencies. To further examine the relationship between response and frequency, we introduce the averaged an-

angular response function averaged over the source locations [27]:

$$R_A(f) = \frac{1}{4\pi} \int_0^{2\pi} \int_0^\pi |F^A|^2 \sin \theta_d d\theta_d d\phi_d, \quad (11)$$

where $A = \{T, V, B, L\}$ denotes four modes independent of ψ . We also introduce effective strain noise to measure the detector's sensitivity to different modes varying with frequency:

$$h_{eff}^A(f) = \sqrt{\frac{S_n(f)}{R_A(f)}}, \quad (12)$$

where $S_n(f)$ is the noise PSD of the detector.

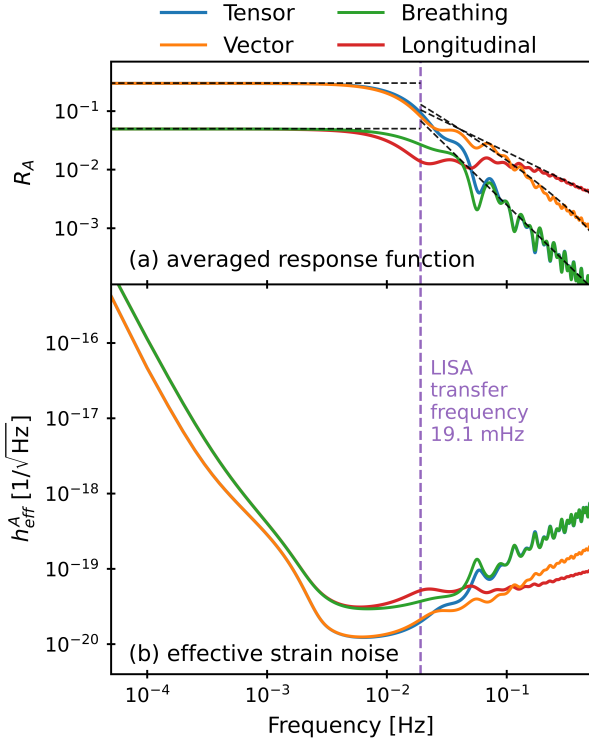


FIG. 6. The averaged response functions $R_A(f)$ and effective strain noise $h_{eff}^A(f)$ of LISA's four modes vary with frequency. We calculate $R_A(f)$ and $h_{eff}^A(f)$ for each frequency point through integration. The purple vertical dashed line represents LISA's transfer frequency $f_* = 19.1$ mHz, and the black dashed line is a fitting approximation of $R_A(f)$ (cf. Ref. [27]).

After our calculations, we derive the averaged response functions and effective strain noise for LISA's four modes, as shown in Fig. 6. At the low-frequency limit, the averaged response function remains constant, with $R_T = R_V = 2(\sin^2 \gamma)/5$ and $R_B = R_L = (\sin^2 \gamma)/15$. As the transfer frequency approaches, R_A starts to decrease, showing three distinct damping trends. R_T and R_V diverge with increasing frequency, similar to R_B and R_L . Additionally, R_T and R_B show differences at the

low-frequency limit. As the frequency increases, the values of those two modes tend to converge. Note that while the average value of these two modes is the same, their responses at individual positions differ, preventing degeneracy between R_T and R_B .

Based on Ref. [27], we analyze the detector's capability to detect various polarizations using the response function. For ground-based detectors, the sensitive frequency band is below the transfer frequency, preventing the distinction between the breathing mode and the longitudinal mode. Space-based detectors, however, can break this degeneracy at non-low-frequency limits. In Sec. V, we simulate GW signals to evaluate the performance of ground- and space-based detectors in constraining polarization.

IV. METHODOLOGY

A. Data analysis

In general, the SNR ρ of GW can be defined as

$$\rho^2 = (h|h), \quad (13)$$

where the inner product $(\cdot|\cdot)$ generalizes the time-domain correlation product and is conventionally defined as

$$(a|b) = 4\text{Re} \left[\int_0^\infty \frac{\tilde{a}^*(f)\tilde{b}(f)}{S_n(f)} df \right], \quad (14)$$

where $\tilde{a}(f)$ and $\tilde{b}(f)$ are the Fourier transforms of $a(t)$ and $b(t)$ respectively. In our study, we consider fourteen GW parameters in total, including ppE parameters, which are

$$\xi = \{t_c, m_1, m_2, z, \iota, \Phi_0, \phi_e, \theta_e, \psi, \alpha_Q, \alpha_D, \alpha_V, \alpha_B, \alpha_L\}, \quad (15)$$

where t_c is the coalescence time, z is the redshift of the source, (ϕ_e, θ_e) is the sky position, representing ecliptic (λ, β) or equatorial (α, δ) coordinates.

For assessing the limitations of the detector on different polarizations and the uncertainty in estimating all parameters, we use the FIM method, defined as

$$\Gamma_{ij} = \left(\frac{\partial h}{\partial \xi_i} \middle| \frac{\partial h}{\partial \xi_j} \right), \quad (16)$$

where ξ_i represents the parameter in Eq. (15). For high SNR, the inverse of the FIM, $\Sigma = \Gamma^{-1}$, is the variance-covariance matrix, with the diagonal elements representing variance [61, 62]. Thus, the uncertainty $\Delta \xi_i$ of the parameters is given by

$$\Delta \xi_i = \sqrt{\Sigma_{ii}}. \quad (17)$$

When calculating the FIM in Eq. (16), we use the numerical differentiation approximation from Refs. [44, 63]. Additionally, for the observation network, the total SNR and FIM are obtained by summing the inner products calculated by each detector.

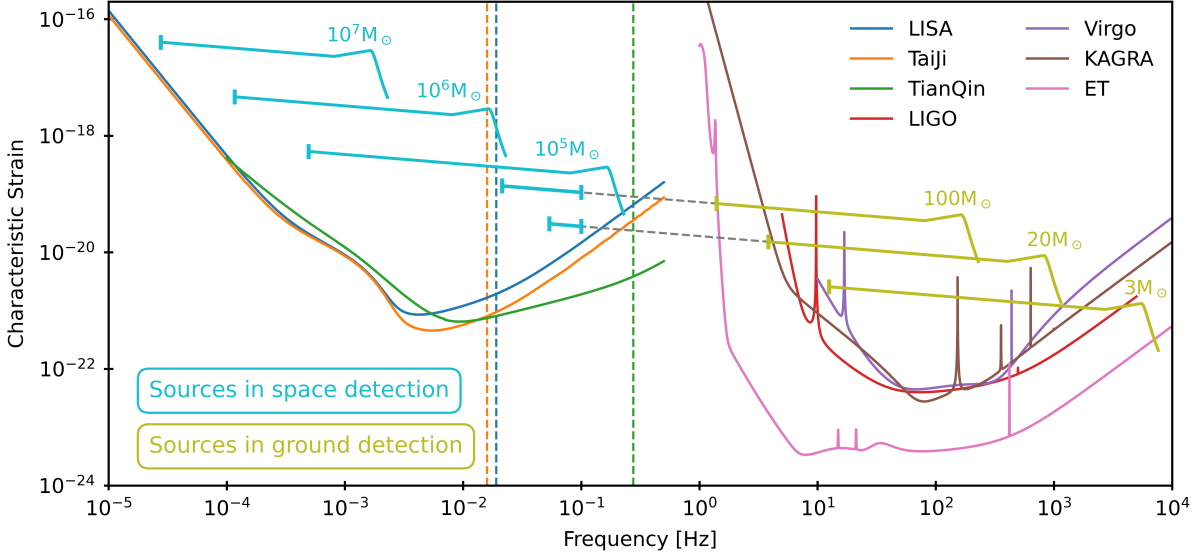


FIG. 7. Multiband observation of BBHs with ground- and space-based detectors. The vertical axis represents the dimensionless characteristic strain $\sqrt{f}S_n(f)$. The BBH curve is derived from Ref. [53] and is intended for illustration purposes only, not for calculation purposes. For luminosity distance selection, we set SBBH at $z = 0.01$ ($D_L = 44.6$ Mpc) and MBHB at $z = 1$ ($D_L = 6.8$ Gpc). The cyan line represents the space detection source, while the olive line represents the ground detection source. The three vertical dashed lines represent the transfer frequencies of the three space-based detectors.

B. BBH source selection

Space- and ground-based detectors have different sensitive frequency bands, resulting in the detection of various GW sources. For BBH sources, ground-based detectors primarily observe SBBHs capturing the complete CBC process of three phases, whereas space-based detectors mainly observe that of MBHBs. Additionally, space-based detectors can detect SBBHs, as many SBBHs inspiral in the low-frequency band before merger, entering the sensitivity band of these detectors. The different BBH sources we selected are presented in Fig. 7.

For all CBC processes, since additional polarizations contribute more significantly in the inspiral phase and Eq. (2) does not apply to the merger and ringdown phases, our waveform model concentrates on the inspiral phase before the binary reaches the innermost stable circular orbit (ISCO). The frequency of ISCO is given by [36]

$$f_{\text{ISCO}} = \frac{c^3}{6\sqrt{6}\pi GM}. \quad (18)$$

Ground-based detectors typically observe SBBH GWs entering the frequency band a few seconds to minutes before merger. Thus, we select three typical SBBHs with equal mass ratios and total masses of $3 M_\odot$, $20 M_\odot$, and $100 M_\odot$, respectively. We calculate the waveforms for the 10 minutes leading up to ISCO. For MBHB sources observed by space-based detectors, we select MBHBs with three typical masses of $10^5 M_\odot$, $10^6 M_\odot$, and $10^7 M_\odot$, calculating waveforms for the 3 months before reaching

ISCO. For multiband observations, we extend two types of SBBHs with masses of $20 M_\odot$ and $100 M_\odot$ to the low-frequency band. Those waveforms last for a year before reaching 0.1 Hz. After 0.1 Hz, those SBBHs would take 3 months ($20 M_\odot$) and 6 days ($100 M_\odot$) to enter the ground-based detector observation frequency band, providing an opportunity to study multiband observations.

TABLE I. Parameter distribution used in calculation [45]. $U[a, b]$ represents a uniform distribution from a to b .

| Parameter | Distribution |
|-------------------------------|-------------------------|
| Ecliptic Longitude λ | $U[0, 2\pi]$ rad |
| Ecliptic Latitude β | $\arcsin(U[-1, 1])$ rad |
| Equatorial Longitude α | $U[0, 2\pi]$ rad |
| Equatorial Latitude δ | $\arcsin(U[-1, 1])$ rad |
| Polarization ψ | $U[0, 2\pi]$ rad |
| Initial Phase ϕ_0 | $U[0, 2\pi]$ rad |

For the selection of sky positions for BBH sources, we use identical parameters for each source, generating 100 distributions consistent with Table I. To study the influence of inclination angle, we consider 45 different inclination angles, resulting in 4500 calculations of SNR and FIM for each BBH source, with the results presented in Secs. V A and V B. Finally, for selecting fiducial values for the ppE parameter, we set it to 10^{-4} (cf. [36]).

V. CONSTRAINTS ON PARAMETERS

A. Results with inclination

We specifically examine the relationship between the uncertainty of ppE parameters and the inclination angle. According to Eq. (2), we can define the distribution of inclination of the tensor mode $p_T(\iota)$ as

$$p_T(\iota) \propto \sqrt{((1 + \cos^2 \iota)/2)^2 + (\cos \iota)^2}. \quad (19)$$

Similarly, we can determine that the distributions of vector mode $p_V(\iota)$ and scalar mode $p_S(\iota)$ are

$$\begin{aligned} p_V(\iota) &\propto \sqrt{(\cos \iota)^2 + 1^2}, \\ p_S(\iota) &\propto \sqrt{(\sin \iota)^2 + (\sin \iota)^2}. \end{aligned} \quad (20)$$

We present the distributions of those three modes in Fig. 8.

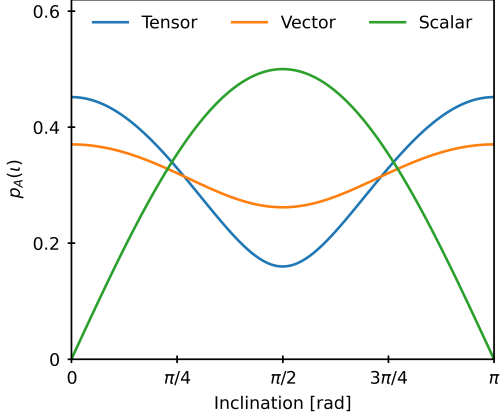


FIG. 8. The distributions of the inclination for tensor mode $p_T(\iota)$, vector mode $p_V(\iota)$ and scalar mode $p_S(\iota)$. All distributions have been normalized.

From Fig. 8, it is evident that the distribution of scalar mode with inclination is opposite to that of tensor and vector modes, reaching its maximum value at $\iota = \pi/2$ and minimum at $\iota = 0, \pi$. From the perspective of inclination angle influence alone, the scalar mode is superior to the other two modes at $\iota = \pi/2$, while tending towards 0 at $\iota = 0, \pi$. Tensor and vector modes exhibit the same trend of change, with tensor modes showing a greater amplitude of variation. Furthermore, we calculate the SNR and FIM to obtain the results for the uncertainty of the ppE parameters, as shown in Fig. 9.

As the distribution in Fig. 8, the variation of the scalar mode with inclination in Fig. 9 is opposite to other modes. Furthermore, due to the distribution of scalar mode being zero at $\iota = 0, \pi$, there is almost no signal near those two values, resulting in the parameter uncertainty of the scalar mode in Fig. 9 approaching infinity. In addition, considering the low-frequency limit, the $\Delta\alpha_B$ and

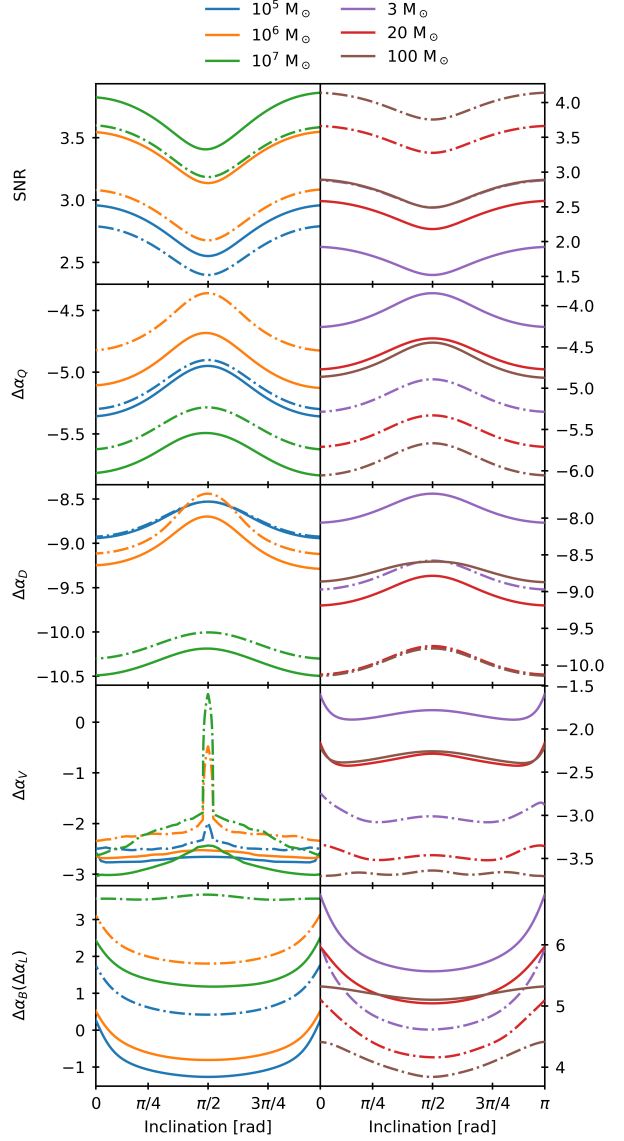


FIG. 9. Relationship between SNR and parameter uncertainty with inclination angle variation. The vertical axis is represented in logarithmic scale. SNR is calculated based on the GR case, and each line in the graph represents the median value. The results for $\Delta\alpha_B$ and $\Delta\alpha_L$ are identical, so only one is shown. The left panel includes LISA (solid line) and TianQin (dashdot line), while the right panel includes LIGO (solid line) and ET (dashdot line).

$\Delta\alpha_L$ of a $10^5 M_\odot$ MBHB with low-SNR are smaller than that of a $10^7 M_\odot$ MBHB with high-SNR. Moreover, due to the superior sensitivity of LISA compared to TianQin and the lower transfer frequency of LISA, the $\Delta\alpha_B$ and $\Delta\alpha_L$ of LISA are significantly better than that of TianQin. For the degeneracy caused by arm length, ground-based detectors cannot distinguish between the breathing mode and the longitudinal mode, so the $\Delta\alpha_B$ and $\Delta\alpha_L$ are much greater than that of space-based detectors and becomes invalid.

Besides the scalar mode, a higher SNR signifies a more robust signal, typically leading to reduced parameter uncertainties. In our calculations, SNR is calculated based on the GR case, where the contribution of tensor modes outweighs that of other modes. Thus, the SNR value is primarily influenced by the tensor modes. In contrast to tensor and scalar modes, the uncertainty of the vector mode is notably higher at $\iota = \pi/2$ in TianQin. This is because TianQin's fixed orientation restricts the response function's variability at that specific angle, leading to a pronounced increase in $\Delta\alpha_V$ near $\iota = \pi/2$.

The transfer frequency not only directly impacts the degeneracy between breathing and longitudinal modes but also affects other aspects. The transfer function \mathcal{T} is directly related to frequency, providing constraints beyond the low-frequency limit. α_Q and α_D determine the variation of the orbital angular frequency, and the influence of \mathcal{T} can reduce parameter uncertainty. Therefore, the $\Delta\alpha_Q$ of $10^5 M_\odot$ MBHB is smaller than that for a $10^6 M_\odot$ MBHB, and $\Delta\alpha_D$ for both MBHBs also varies with the relationship near $\iota = \pi/2$. Because of the low-frequency limit, ground-based detectors are not affected by \mathcal{T} , causing the uncertainties $\Delta\alpha_Q$ and $\Delta\alpha_D$ for SBBHs to depend entirely on SNR. This section focuses on presenting and analyzing the relationship between the uncertainty of ppE parameters and the inclination angle for two typical space-based and ground-based detectors.

B. Results with ppE parameters

We evaluate the performance of several typical BBHs using different detectors and various parameters. The results for different detectors and their networks are illustrated in Fig. 10.

Regarding space-based detectors, Taiji, which shares a similar configuration with LISA, surpasses LISA across all metrics, demonstrating superior SNR and reduced parameter uncertainty. Moreover, TianQin's distinct orbital configuration results in inferior performance compared to LISA and Taiji. Additionally, the significant rise in TianQin's parameter uncertainty at $\iota = \pi/2$, particularly in $\Delta\alpha_V$, leads to the upper limit of the box plot for $\Delta\alpha_V$ being substantially higher than its median value in the comprehensive results presented in Fig. 10.

When considering the space-based detector network, significant improvements are observed across all metrics compared to individual detectors. Since both LISA and Taiji utilize heliocentric orbits, their network configuration remains stable, maintaining a consistent angle between the detectors. LISA and the three alternative orbital configurations of Taiji exhibit different angles, which introduce variations in the outcomes. A larger angular separation between the detectors correlates with greater coverage of the sky area with high sensitivity, resulting in differences in parameter uncertainty under similar SNR conditions. Overall, the LISA+TJm configuration achieves the most favorable results, with

LISA+TJp surpassing LISA+TJc, especially noticeable in parameters like $\Delta\alpha_V$ and $\Delta\Omega$. Moreover, it is evident that the LISA+TJ combination outperforms LISA+TQ, and a network of three detectors surpasses two. For more detailed analysis of space detector networks, refer to Ref. [44].

Single ground-based detectors such as Virgo and KAGRA do not perform well in detecting additional polarization parameters and accurately determining the sky position of the source. This limitation arises because a single detector has only one response angle, and a 10-minute GW signal is relatively short compared to the ground-based detector's observational period (Earth's rotation period). In the ground-based detector's coordinate system, a 10-minute SBBH source travels only 2.5° , whereas a 90-day MBHB source moves nearly 90° in the space-based detector coordinate system. Consequently, the parameter uncertainty range for ground-based detectors is larger. Furthermore, both LIGO and ET have three detectors, but ET detectors are all coplanar, whereas LIGO's are not. This situation is similar to the superiority of LISA+TJm over LISA+TJc, where the relative positions of LIGO's three detectors offer greater advantages compared to ET. Therefore, despite the SNR of ET is one order of magnitude higher than LIGO, their $\Delta\Omega$ values are still very similar.

Regarding the ground-based detector network, currently operational LVK cannot fully compensate for the sensitivity differences between second-generation and third-generation detectors. Compared to ET, LVK exhibits a difference of one to two orders of magnitude in the limitations of ppE parameters. Moreover, due to the varied response angles of LVK, $\Delta\Omega$ values are slightly better than those of ET. The LVK+ET combination is the most comprehensive, significantly enhancing network sensitivity. For instance, $\Delta\alpha_Q$ and $\Delta\alpha_D$ can approach the sensitivity level of space-based detector networks, with $\Delta\alpha_V$ potentially surpassing them. Due to the arm length, the $\Delta\alpha_B$ and $\Delta\alpha_L$ of the ground-based detector network is four to six orders of magnitude higher than that of the space-based detector network, making it impossible to distinguish between breathing and longitudinal modes.

C. Results with redshift

In our previous calculations and analysis, we assume fixed redshift: $z = 0.01$ for SBBH and $z = 1$ for MBHB. Different redshifts also lead to variations in the GW signal, potentially impacting the final results. From Eq. (2), the strain is inversely proportional to the luminosity distance, represented as $h \propto 1/D_L \sim 1/z$. Roughly speaking, as redshift increases, the strain decreases. Regarding the ppE parameter ξ , the partial derivative of the strain with respect to it, $\partial h / \partial \xi \propto 1/z$. Consequently, the FIM is $(\partial h / \partial \xi | \partial h / \partial \xi) \propto 1/z^2$, and thus the uncertainty of the ppE parameter scales as $\Delta\xi \propto z$. In other words, the

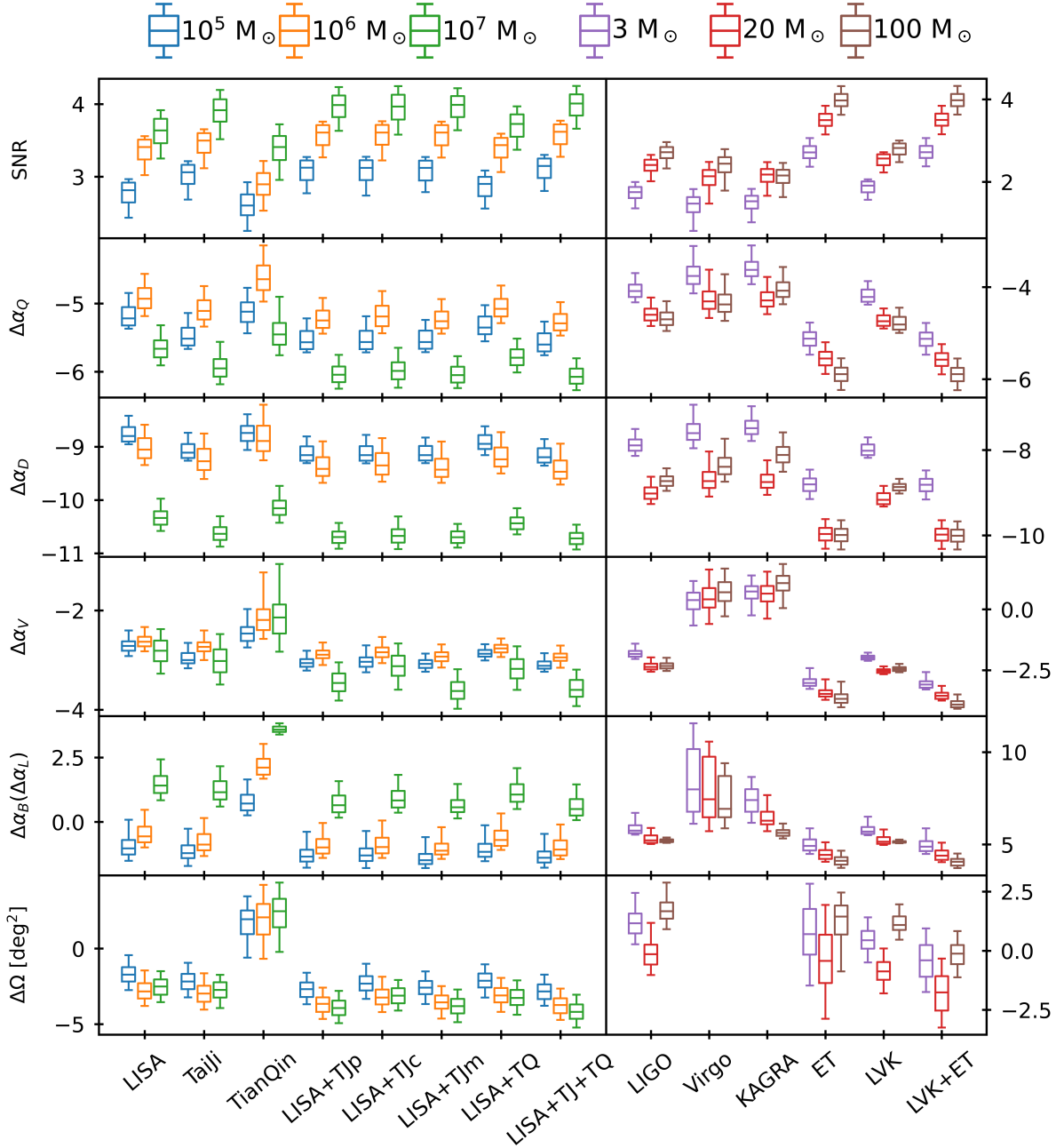


FIG. 10. SNR and parameter uncertainty with space- and ground-based detectors. The vertical axis is represented in logarithmic scale. The upper and lower horizontal lines in each box represent the 90% confidence interval. The edges of the box correspond to the upper and lower quartiles, while the lines inside the box represent the median. The uncertainty of sky position is expressed as $\Delta\Omega = 2\pi|\sin\theta_e|(\Sigma_{\theta_e\theta_e}\Sigma_{\phi_e\phi_e} - \Sigma_{\theta_e\phi_e}^2)^{1/2}$ [64]. The left panel shows the results for the space-based detectors, where TJ represents Taiji and TQ represents TianQin. In our calculations, there is no difference between the two alternative orbital configurations for TianQin, so they are not labeled separately. The right panel displays the results for the ground-based detectors, but due to the extremely poor positioning capabilities of individual Virgo and KAGRA detectors, their $\Delta\Omega$ values are not shown.

uncertainty of the ppE parameter is directly proportional to the redshift:

$$\Delta\xi(z) = \mathcal{K}z + \Delta\xi(0), \quad (21)$$

where \mathcal{K} is a proportionality constant. We calculate the results for SBBH and MBHB at different redshifts, as shown in Table II.

From Eq. (21), it is clear that the uncertainty of the

TABLE II. Proportional coefficient \mathcal{K} corresponding to different ppE parameters. We use logarithmic $\log(\mathcal{K})$ to represent the results in the table.

| Detector | $M[M_\odot]$ | $\Delta\alpha_Q$ | $\Delta\alpha_D$ | $\Delta\alpha_V$ | $\Delta\alpha_B(\alpha_L)$ |
|----------|--------------|------------------|------------------|------------------|----------------------------|
| LISA | 10^5 | -5.01 | -8.59 | -2.50 | -0.82 |
| | 10^6 | -4.72 | -8.84 | -2.42 | -0.35 |
| | 10^7 | -5.45 | -10.13 | -2.60 | 1.62 |
| Taiji | 10^5 | -5.30 | -8.90 | -2.79 | -1.00 |
| | 10^6 | -4.90 | -9.06 | -2.52 | -0.66 |
| | 10^7 | -5.74 | -10.42 | -2.81 | 1.36 |
| TianQin | 10^5 | -4.91 | -8.53 | -2.25 | 0.92 |
| | 10^6 | -4.43 | -8.68 | -1.98 | 2.32 |
| | 10^7 | -5.24 | -9.95 | -1.93 | 3.79 |
| LIGO | 3 | -1.90 | -5.71 | 0.35 | 7.93 |
| | 20 | -2.42 | -6.83 | -0.18 | 7.41 |
| | 100 | -2.52 | -6.54 | -0.15 | 7.38 |
| Virgo | 3 | -1.58 | -5.42 | 2.56 | 10.09 |
| | 20 | -2.13 | -6.55 | 2.60 | 9.59 |
| | 100 | -2.19 | -6.21 | 2.88 | 9.18 |
| KAGRA | 3 | -1.44 | -5.30 | 2.91 | 9.59 |
| | 20 | -2.11 | -6.57 | 2.82 | 8.44 |
| | 100 | -1.89 | -5.93 | 3.26 | 7.80 |
| ET | 3 | -2.94 | -6.62 | -0.85 | 7.08 |
| | 20 | -3.37 | -7.78 | -1.29 | 6.62 |
| | 100 | -3.71 | -7.81 | -1.49 | 6.30 |

ppE parameters is proportional to the redshift. Additionally, the rate of change in uncertainty with redshift varies for different ppE parameters. Table II illustrates that the influence of redshift on $\Delta\alpha_Q$ and $\Delta\alpha_D$ is negligible, as most \mathcal{K} values are less than 10^{-4} . That is because these two parameters are directly related to frequency, and the change in GW amplitude due to redshift has a negligible effect on frequency resolution. Moreover, ground-based detectors exhibit relatively larger \mathcal{K} values compared to space-based detectors.

The \mathcal{K} for $\Delta\alpha_V$ is significantly larger compared to the first two parameters. Space-based detectors typically have \mathcal{K} values around 10^{-2} . In contrast, ground-based detectors like Virgo and KAGRA have \mathcal{K} values around 10^2 . LIGO and ET perform better, with $\mathcal{K} < 1$ in most cases. Those observations are consistent with the analysis in last section, explaining these differences based on detector performance.

Due to the degeneracy in ground-based detectors, $\Delta\alpha_B$ ($\Delta\alpha_L$) exhibits significantly large \mathcal{K} values, exceeding 10^6 . In contrast, space-based detectors, which break this degeneracy, yield noticeably better results. The re-

lationship between the frequency range of MBHBs and the transfer frequency determines the results in Table II. Smaller mass MBHBs exhibit lower frequencies closer to the transfer frequency, enhancing the resolution of these two modes and leading to smaller \mathcal{K} values. The results are similar for different detectors: Taiji has the smallest transfer frequency, while TianQin has the largest, corresponding to their respective \mathcal{K} values.

D. Multiband observation

Space-based detectors can not only observe MBHBs, but also SBBHs. Among tens of thousands of sources, a small number of SBBHs increase in frequency rapidly and merge into the ground-based detector frequency band within a short period, enabling multiband observations by both space- and ground-based detectors [65]. We calculate FIM for two typical SBBHs observed across multiple frequency bands and compared their results with those observed only by ground-based detectors, as shown in Fig. 11.

Multiband observations provide a significant enhancement to ground-based detectors, particularly in resolving the degeneracy between the breathing and longitudinal modes. The addition of space-based detectors effectively breaks the degeneracy, allowing multiband SBBH observations to limit $\Delta\alpha_B$ and $\Delta\alpha_L$ to levels comparable with space-based detector observations of MBHB. Additionally, multiband observations greatly improve the performance of Virgo and KAGRA in $\Delta\alpha_V$, reducing them by nearly three orders of magnitude, approaching the levels achieved by LIGO and ET. Furthermore, the $\Delta\alpha_V$ level of the ground-based detector network remains higher than that of the space-based detector network, so the improvement from multiband observations is not as significant.

Regarding $\Delta\alpha_Q$ and $\Delta\alpha_D$, multiband observations have varying improvements for SBBH depending on the mass. The results for SBBH with $M = 20 M_\odot$ do not show significant improvement, while those for $M = 100 M_\odot$ show some improvement. Due to the high sensitivity of ET, multiband observation does not significantly improve ET and LVK+ET, it significantly enhances the performance of only second-generation detectors. Within the space-based detector frequency band, although both types of SBBH have a duration of one year, their frequency variation ranges differ. Specifically, the frequency variation for $M = 20 M_\odot$ SBBHs is 46 mHz, whereas for $M = 100 M_\odot$ it increases to 78 mHz. Greater frequency variations lead to stronger constraints, thereby affecting the observed improvements. Moreover, longer observation times result in larger frequency variations. While four-year observations generally outperform one-year observations, this improvement is not significant. This is because the further away from the merger, the smaller the frequency change over the same time period. For example, in calculations for SBBH with $M = 100 M_\odot$,

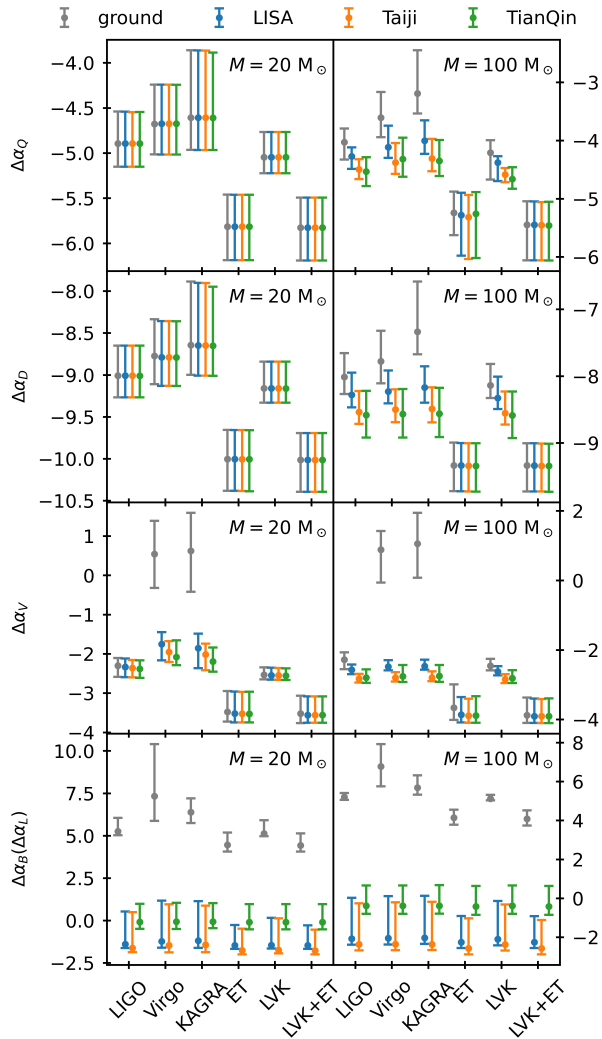


FIG. 11. The uncertainty of ppE parameters in multiband observations. The vertical axis is represented in logarithmic scale. For simplicity, we use points to represent the median, with error bars above and below indicating the 90% confidence interval. In the left panel, the total mass of the SBBH source is $M = 20 M_{\odot}$, while in the right panel, it is $M = 100 M_{\odot}$. To save computational resources, only a subset of the sources are calculated, resulting in slight differences from Fig. 10.

the frequency change in one year leading up to 0.1 Hz is 78 mHz, but the change over four years is only 87 mHz, indicating a minimal additional change of 9 mHz over three years. Hence, our choice of a one-year observation duration remains reasonable.

The performance of different space-based detectors significantly affects the results of multi band observations, for example, Taiji is superior to LISA. Moreover, the selected cutoff frequency of SBBHs within the space-based detector band is 0.1 Hz, lower than TianQin's 0.28 Hz transfer frequency. That disparity renders TianQin less effective than LISA and Taiji in observing breathing and longitudinal modes, resulting in a multiband observation

improvement for $\Delta\alpha_B$ and $\Delta\alpha_L$ that is two orders of magnitude weaker compared to the other detectors. Conversely, TianQin exhibits significantly enhanced multiband observations for $\Delta\alpha_Q$, $\Delta\alpha_D$, and $\Delta\alpha_V$, because TianQin's sensitivity within the selected SBBH frequency band surpasses that of the other detectors, leading to superior results. Overall, the addition of space-based detectors compensates for the degeneracy of ground-based detectors in scalar modes and also improves other aspects, enabling the observation results of SBBH to reach the level of MBHB results.

E. Multimessenger observation

Apart from multiband observations using space- and ground-based detectors, multimessenger observations, which include the assistance of electromagnetic (EM) observations, can similarly enhance the performance of GW observations. EM observations offer a unique perspective about BBH sources distinct from GW observations. References [66–69] have demonstrated that mergers of MBHBs can emit EM radiation from accretion disks, while mergers of SBBHs in active galactic nuclei can produce jets, making both scenarios promising targets for EM detectors. Accurate determination of the source's sky position enables subsequent EM follow-up observations to search for counterparts. The results of EM observations can then serve as valuable priors to reduce uncertainties in GW observations.

The EM effects produced by BBH mergers are expected to be detected by infrared, optical, and X-ray observatories, and the results from these observatories have different impacts on the enhancement of GW. For simplicity, we consider an ideal scenario where EM observations accurately determine specific parameters, ignoring differences between EM detectors. According to Refs. [44, 63], when considering the improvement from EM observations, the corresponding row and column in the FIM are removed to reduce the uncertainties of other parameters in the GW data. That method assesses the performance enhancement of GW observations under ideal multimessenger conditions. We quantify these enhancements when EM observations perfectly determine redshift, sky position, or inclination angle, comparing them against results from GW observations alone. Notably, although this study only focus on ppE parameters, multimessenger observations also offer varying degrees of enhancement for time, mass, polarization, and other parameters. For details on enhancements in non-ppE parameters, refer to Ref. [44].

For LISA and Taiji, multimessenger observations demonstrate notable enhancements primarily for MBHBs with $M = 10^7 M_{\odot}$. Determining the redshift or inclination angle through multimessenger observations can reduce $\Delta\alpha_V$, $\Delta\alpha_B$, and $\Delta\alpha_L$ by 15% to 24%. Determining the sky position can reduce these parameters by 36% to 49%. Multimessenger observations yield even more sig-

nificant improvements for TianQin, enhancing detection capabilities across all three typical MBHB masses. When the redshift, inclination angle, or sky position is accurately determined, $\Delta\alpha_V$ can be reduced by 40% to 57%. Furthermore, due to arm length, reductions in $\Delta\alpha_B$ and $\Delta\alpha_L$ are more modest, ranging from 9% to 17%.

For ground-based detectors, the impact of multimesenger observations on $\Delta\alpha_B$ and $\Delta\alpha_L$ is considerably smaller compared to multiband observations, as it does not resolve the degeneracy and thus is not considered further. LIGO shows less significant improvement compared to ET, due to its less diverse response angles. Determining the redshift or inclination angle results in a reduction of $\Delta\alpha_V$ by 5% to 7%, with negligible changes observed when determining the sky position. In contrast, ET exhibits more substantial enhancements. When any one of the three parameters is determined, $\Delta\alpha_V$ can be reduced by 15% to 43%, with larger reductions for higher-mass SBBHs. Moreover, multimesenger observations yield remarkable improvements for Virgo and KAGRA, achieving reductions in $\Delta\alpha_V$ by 97% to 99.4%. This improvement is only one order of magnitude lower than that of LIGO and significantly surpasses the outcomes from GW observations alone.

Multimesenger observations, whether for space- or ground-based detectors, do not improve the other two ppE parameters, $\Delta\alpha_Q$ and $\Delta\alpha_D$. That is because these two ppE parameters are directly tied to GW frequency, where GW observation precision is highest. Theoretically, multimesenger observations could enhance constraints on all ppE parameters, but in practice, some improvements are too marginal. Therefore, we only present results where the parameter uncertainty is reduced by more than 5%, with most unreported results being less than 1%. In summary, multimesenger observations can moderately enhance the performance of GW observations, providing stronger constraints on ppE parameters.

VI. CONCLUSION

In this paper, we investigate the expected targets for constraining GW polarization using space- and ground-based detectors within the ppE framework. Specifically, we adopt a model-independent ppE framework that incorporates a GW waveform with all six polarization modes, adhering to current GR test results. For space-based detectors, we consider LISA, Taiji, and TianQin, along with alternative orbital configurations, both individually and in network scenarios. For ground-based detectors, we include the currently operational LVK and the third-generation detector ET, evaluated both individually and in network. Our analysis focuses on detector performance across different polarization modes, emphasizing the response function's perspective. Furthermore, by simulating three typical masses of MBHB and SBBH, we use the FIM to quantify ppE parameter constraints for both space- and ground-based detectors, presenting

the results under different combinations. Furthermore, we explore how multiband and multimesenger observations enhance ppE constraints, offering a comprehensive analysis from diverse angles.

For space-based detectors, Taiji provides the best constraints on GW polarization modes, with LISA performing better than TianQin. Specifically, TianQin's constraints on scalar modes are significantly weaker than those of LISA and Taiji, while the uncertainties in other ppE parameters among the three detectors differ by less than an order of magnitude. In network scenarios, the combination of LISA+TJm performs slightly better than other combinations, and the network of all three detectors outperforms two-detector networks.

For ground-based detectors, the differences in constraints on frequency-related ppE parameters are minor, but LIGO's results for vector modes are substantially better than those of Virgo and KAGRA, approaching the level of ET. In network scenarios, the LVK combination does not surpass the results of ET alone, with the LVK+ET network providing the best constraints. Overall, ground-based detectors are unable to distinguish between breathing and longitudinal modes and are significantly less capable of constraining scalar modes compared to space detectors. Other than this, the constraints on ppE parameters from space- and ground-based detectors are comparable.

For multiband observation, it can effectively break the degeneracies of ground-based detectors in breathing and longitudinal modes, addressing the inability of ground detectors to distinguish scalar modes. They also improve the ability of Virgo and KAGRA to constrain vector modes, reaching the level of LIGO, and offer certain improvements for other ppE parameters. Moreover, TianQin brings the greatest improvement, followed by Taiji, and LISA has the least improvement.

For multimesenger observation, it provides the most significant enhancement for TianQin, bringing its results for vector modes close to those of LISA. For scalar modes, LISA and Taiji see greater improvements. ET shows a larger improvement compared to LIGO, and Virgo and KAGRA experience substantial enhancements, with their results for vector modes approaching the level of LIGO. Overall, both multiband and multimesenger observations can enhance GW detection results to a certain extent, leading to better constraints on GW polarization modes.

In future research, we plan to approach the study from several aspects. First, we will use longer-duration GW signals, which can contain more information, and consider the non-light-speed propagation caused by different modes, where vector and scalar modes may arrive before or simultaneously with tensor modes [70]. Second, we aim to delve into the effects brought by Time-Delay Interferometry (TDI) technology, as different TDI combinations may result in subtle differences in the outcomes [71]. Additionally, we will consider various sources, examining the impact of ppE parameters on unequal mass BBH sys-

tems. Lastly, in the context of multimessenger observations, we will study the performance of EM detectors under realistic conditions, providing results that are more aligned with actual scenarios to enhance GW observations. In summary, through these in-depth studies, we aim to advance the research on GW polarization modes, evaluate detector performance more comprehensively and in greater detail, and provide more valuable results.

ACKNOWLEDGMENTS

This work was supported by the National Key Research and Development Program of China (Grant

No. 2021YFC2203004), the National Natural Science Foundation of China (Grant No. 12347101), and the Natural Science Foundation of Chongqing (Grant No. CSTB2023NSCQ-MSX0103).

-
- [1] I. H. Stairs, Testing general relativity with pulsar timing, *Living Rev. Rel.* **6**, 5 (2003), arXiv:astro-ph/0307536.
 - [2] C. M. Will, The Confrontation between General Relativity and Experiment, *Living Rev. Rel.* **17**, 4 (2014), arXiv:1403.7377 [gr-qc].
 - [3] T. Baker, D. Psaltis, and C. Skordis, Linking Tests of Gravity On All Scales: from the Strong-Field Regime to Cosmology, *Astrophys. J.* **802**, 63 (2015), arXiv:1412.3455 [astro-ph.CO].
 - [4] T. Clifton, P. G. Ferreira, A. Padilla, and C. Skordis, Modified Gravity and Cosmology, *Phys. Rept.* **513**, 1 (2012), arXiv:1106.2476 [astro-ph.CO].
 - [5] E. Berti *et al.*, Testing General Relativity with Present and Future Astrophysical Observations, *Class. Quant. Grav.* **32**, 243001 (2015), arXiv:1501.07274 [gr-qc].
 - [6] C. Shi, M. Ji, J.-d. Zhang, and J. Mei, Testing general relativity with TianQin: The prospect of using the inspiral signals of black hole binaries, *Phys. Rev. D* **108**, 024030 (2023), arXiv:2210.13006 [gr-qc].
 - [7] D. M. Eardley, D. L. Lee, A. P. Lightman, R. V. Wagoner, and C. M. Will, Gravitational-wave observations as a tool for testing relativistic gravity, *Phys. Rev. Lett.* **30**, 884 (1973).
 - [8] C. Brans and R. H. Dicke, Mach's principle and a relativistic theory of gravitation, *Phys. Rev.* **124**, 925 (1961).
 - [9] M. E. S. Alves, O. D. Miranda, and J. C. N. de Araujo, Probing the f(R) formalism through gravitational wave polarizations, *Phys. Lett. B* **679**, 401 (2009), arXiv:0908.0861 [gr-qc].
 - [10] H. Rizwana Kausar, L. Philippoz, and P. Jetzer, Gravitational Wave Polarization Modes in $f(R)$ Theories, *Phys. Rev. D* **93**, 124071 (2016), arXiv:1606.07000 [gr-qc].
 - [11] T. Kobayashi, Horndeski theory and beyond: a review, *Rept. Prog. Phys.* **82**, 086901 (2019), arXiv:1901.07183 [gr-qc].
 - [12] T. Jacobson and D. Mattingly, Einstein-Aether waves, *Phys. Rev. D* **70**, 024003 (2004), arXiv:gr-qc/0402005.
 - [13] K. Lin, X. Zhao, C. Zhang, T. Liu, B. Wang, S. Zhang, X. Zhang, W. Zhao, T. Zhu, and A. Wang, Gravitational waveforms, polarizations, response functions, and energy losses of triple systems in Einstein-aether theory, *Phys. Rev. D* **99**, 023010 (2019), arXiv:1810.07707 [astro-ph.GA].
 - [14] J. D. Bekenstein, Relativistic gravitation theory for the MOND paradigm, *Phys. Rev. D* **70**, 083509 (2004), [Erratum: Phys.Rev.D 71, 069901 (2005)], arXiv:astro-ph/0403694.
 - [15] Y. Gong and S. Hou, The Polarizations of Gravitational Waves, *Universe* **4**, 85 (2018), arXiv:1806.04027 [gr-qc].
 - [16] B. P. Abbott *et al.* (LIGO Scientific, Virgo), Observation of Gravitational Waves from a Binary Black Hole Merger, *Phys. Rev. Lett.* **116**, 061102 (2016), arXiv:1602.03837 [gr-qc].
 - [17] B. P. Abbott *et al.* (LIGO Scientific, Virgo), GWTC-1: A Gravitational-Wave Transient Catalog of Compact Binary Mergers Observed by LIGO and Virgo during the First and Second Observing Runs, *Phys. Rev. X* **9**, 031040 (2019), arXiv:1811.12907 [astro-ph.HE].
 - [18] R. Abbott *et al.* (LIGO Scientific, Virgo), GWTC-2: Compact Binary Coalescences Observed by LIGO and Virgo During the First Half of the Third Observing Run, *Phys. Rev. X* **11**, 021053 (2021), arXiv:2010.14527 [gr-qc].
 - [19] R. Abbott *et al.* (LIGO Scientific, Virgo), GWTC-3: Compact Binary Coalescences Observed by LIGO and Virgo During the Second Part of the Third Observing Run (2023), arXiv:2111.03606 [gr-qc].
 - [20] B. P. Abbott *et al.* (LIGO Scientific, Virgo), Tests of General Relativity with the Binary Black Hole Signals from the LIGO-Virgo Catalog GWTC-1, *Phys. Rev. D* **100**, 104036 (2019), arXiv:1903.04467 [gr-qc].
 - [21] R. Abbott *et al.* (LIGO Scientific, Virgo), Tests of general relativity with binary black holes from the second LIGO-Virgo gravitational-wave transient catalog, *Phys. Rev. D* **103**, 122002 (2021), arXiv:2010.14529 [gr-qc].
 - [22] T. L. S. Collaboration, the Virgo Collaboration, and the KAGRA Collaboration, Tests of general relativity with gwtc-3 (2021), arXiv:2112.06861 [gr-qc].
 - [23] B. P. Abbott *et al.* (LIGO Scientific, Virgo), Tests of general relativity with GW150914, *Phys. Rev. Lett.* **116**, 221101 (2016), [Erratum: Phys.Rev.Lett. 121, 129902 (2018)], arXiv:1602.03841 [gr-qc].
 - [24] B. P. Abbott *et al.* (LIGO Scientific, Virgo), Tests of General Relativity with GW170817, *Phys. Rev. Lett.* **123**, 011102 (2019), arXiv:1811.00364 [gr-qc].
 - [25] E. Berti, K. Yagi, and N. Yunes, Extreme Gravity Tests with Gravitational Waves from Compact Binary Coalescences: (I) Inspiral-Merger, *Gen. Rel. Grav.* **50**, 46

- (2018), arXiv:1801.03208 [gr-qc].
- [26] E. Berti, K. Yagi, H. Yang, and N. Yunes, Extreme Gravity Tests with Gravitational Waves from Compact Binary Coalescences: (II) Ringdown, *Gen. Rel. Grav.* **50**, 49 (2018), arXiv:1801.03587 [gr-qc].
- [27] D. Liang, Y. Gong, A. J. Weinstein, C. Zhang, and C. Zhang, Frequency response of space-based interferometric gravitational-wave detectors, *Phys. Rev. D* **99**, 104027 (2019), arXiv:1901.09624 [gr-qc].
- [28] J. Aasi *et al.* (LIGO Scientific), Advanced LIGO, *Class. Quant. Grav.* **32**, 074001 (2015), arXiv:1411.4547 [gr-qc].
- [29] F. Acernese *et al.* (VIRGO), Advanced Virgo: a second-generation interferometric gravitational wave detector, *Class. Quant. Grav.* **32**, 024001 (2015), arXiv:1408.3978 [gr-qc].
- [30] K. Somiya (KAGRA), Detector configuration of KAGRA: The Japanese cryogenic gravitational-wave detector, *Class. Quant. Grav.* **29**, 124007 (2012), arXiv:1111.7185 [gr-qc].
- [31] P. Amaro-Seoane, H. Audley, S. Babak, J. Baker, E. Barausse, P. Bender, E. Berti, P. Binetruy, M. Born, D. Bortoluzzi, *et al.*, Laser interferometer space antenna, arXiv preprint arXiv:1702.00786 (2017).
- [32] W.-R. Hu and Y.-L. Wu, The Taiji Program in Space for gravitational wave physics and the nature of gravity, *Natl. Sci. Rev.* **4**, 685 (2017).
- [33] J. Luo *et al.* (TianQin), TianQin: a space-borne gravitational wave detector, *Class. Quant. Grav.* **33**, 035010 (2016), arXiv:1512.02076 [astro-ph.IM].
- [34] J. R. Gair, M. Vallisneri, S. L. Larson, and J. G. Baker, Testing General Relativity with Low-Frequency, Space-Based Gravitational-Wave Detectors, *Living Rev. Rel.* **16**, 7 (2013), arXiv:1212.5575 [gr-qc].
- [35] N. Yunes and F. Pretorius, Fundamental Theoretical Bias in Gravitational Wave Astrophysics and the Parameterized Post-Einsteinian Framework, *Phys. Rev. D* **80**, 122003 (2009), arXiv:0909.3328 [gr-qc].
- [36] C. Liu, W.-H. Ruan, and Z.-K. Guo, Constraining gravitational-wave polarizations with Taiji, *Phys. Rev. D* **102**, 124050 (2020), arXiv:2006.04413 [gr-qc].
- [37] K. Chatzioannou, N. Yunes, and N. Cornish, Model-Independent Test of General Relativity: An Extended post-Einsteinian Framework with Complete Polarization Content, *Phys. Rev. D* **86**, 022004 (2012), [Erratum: Phys.Rev.D 95, 129901 (2017)], arXiv:1204.2585 [gr-qc].
- [38] S. Tahura and K. Yagi, Parameterized Post-Einsteinian Gravitational Waveforms in Various Modified Theories of Gravity, *Phys. Rev. D* **98**, 084042 (2018), [Erratum: Phys.Rev.D 101, 109902 (2020)], arXiv:1809.00259 [gr-qc].
- [39] N. Yunes and X. Siemens, Gravitational-Wave Tests of General Relativity with Ground-Based Detectors and Pulsar Timing-Arrays, *Living Rev. Rel.* **16**, 9 (2013), arXiv:1304.3473 [gr-qc].
- [40] T. Narikawa and H. Tagoshi, The potential of advanced ground-based gravitational wave detectors to detect generic deviations from general relativity, *PTEP* **2016**, 093E02 (2016), arXiv:1601.07691 [gr-qc].
- [41] C. Huwyler, E. K. Porter, and P. Jetzer, Supermassive Black Hole Tests of General Relativity with eLISA, *Phys. Rev. D* **91**, 024037 (2015), arXiv:1410.8815 [gr-qc].
- [42] R. Nair, S. Jhingan, and T. Tanaka, Synergy between ground and space based gravitational wave detectors for estimation of binary coalescence parameters, *PTEP* **2016**, 053E01 (2016), arXiv:1504.04108 [gr-qc].
- [43] G. Wang and W.-B. Han, Observing gravitational wave polarizations with the LISA-TAIJI network, *Phys. Rev. D* **103**, 064021 (2021), arXiv:2101.01991 [gr-qc].
- [44] J. Wu and J. Li, Subtraction of the confusion foreground and parameter uncertainty of resolvable galactic binaries on the networks of space-based gravitational-wave detectors, *Phys. Rev. D* **108**, 124047 (2023), arXiv:2307.05568 [gr-qc].
- [45] J. Wu, J. Li, X. Liu, and Z. Cao, Comparison and application of different post-Newtonian models for inspiralling stellar-mass binary black holes with space-based GW detectors, *Phys. Rev. D* **109**, 104014 (2024), arXiv:2401.03113 [gr-qc].
- [46] J. Wu, J. Li, and Q.-Q. Jiang, Application of Newtonian approximate model to LIGO gravitational wave data processing, *Chin. Phys. B* **32**, 090401 (2023).
- [47] D. Hansen, N. Yunes, and K. Yagi, Projected Constraints on Lorentz-Violating Gravity with Gravitational Waves, *Phys. Rev. D* **91**, 082003 (2015), arXiv:1412.4132 [gr-qc].
- [48] K. G. Arun, Generic bounds on dipolar gravitational radiation from inspiralling compact binaries, *Class. Quant. Grav.* **29**, 075011 (2012), arXiv:1202.5911 [gr-qc].
- [49] L. O’Beirne, N. J. Cornish, S. J. Vigeland, and S. R. Taylor, Constraining alternative polarization states of gravitational waves from individual black hole binaries using pulsar timing arrays, *Phys. Rev. D* **99**, 124039 (2019), arXiv:1904.02744 [gr-qc].
- [50] LIGO Scientific Collaboration, Virgo Collaboration, and KAGRA Collaboration, *LVK Algorithm Library - LALSuite*, Free software (GPL) (2018).
- [51] K. Wette, SWIGLAL: Python and Octave interfaces to the LALSuite gravitational-wave data analysis libraries, *SoftwareX* **12**, 100634 (2020).
- [52] P. Murdin, ed., *Encyclopedia of Astronomy & Astrophysics*, 1st ed. (CRC Press, 2001) <https://doi.org/10.1201/9781003220435>.
- [53] T. Robson, N. J. Cornish, and C. Liu, The construction and use of LISA sensitivity curves, *Class. Quant. Grav.* **36**, 105011 (2019), arXiv:1803.01944 [astro-ph.HE].
- [54] Z. Ren, T. Zhao, Z. Cao, Z.-K. Guo, W.-B. Han, H.-B. Jin, and Y.-L. Wu, Taiji data challenge for exploring gravitational wave universe, *Front. Phys. (Beijing)* **18**, 64302 (2023), arXiv:2301.02967 [gr-qc].
- [55] X.-C. Hu, X.-H. Li, Y. Wang, W.-F. Feng, M.-Y. Zhou, Y.-M. Hu, S.-C. Hu, J.-W. Mei, and C.-G. Shao, Fundamentals of the orbit and response for TianQin, *Class. Quant. Grav.* **35**, 095008 (2018), arXiv:1803.03368 [gr-qc].
- [56] M. Punturo *et al.*, The Einstein Telescope: A third-generation gravitational wave observatory, *Class. Quant. Grav.* **27**, 194002 (2010).
- [57] S.-X. Yi, G. Nelemans, C. Brinkerink, Z. Kostrzewa-Rutkowska, S. T. Timmer, F. Stoppa, E. M. Rossi, and S. F. Portegies Zwart, The Gravitational Wave Universe Toolbox - A software package to simulate observations of the gravitational wave universe with different detectors, *Astron. Astrophys.* **663**, A155 (2022), arXiv:2106.13662 [astro-ph.HE].
- [58] S. Hild *et al.*, Sensitivity Studies for Third-Generation Gravitational Wave Observatories, *Class. Quant. Grav.* **28**, 094013 (2011), arXiv:1012.0908 [gr-qc].
- [59] A. Nishizawa, A. Taruya, K. Hayama, S. Kawamura, and M.-a. Sakagami, Probing non-tensorial polarizations of

- stochastic gravitational-wave backgrounds with ground-based laser interferometers, *Phys. Rev. D* **79**, 082002 (2009), arXiv:0903.0528 [astro-ph.CO].
- [60] N. J. Cornish and S. L. Larson, Space missions to detect the cosmic gravitational wave background, *Class. Quant. Grav.* **18**, 3473 (2001), arXiv:gr-qc/0103075.
- [61] S. Shah, M. van der Sluys, and G. Nelemans, Using electromagnetic observations to aid gravitational-wave parameter estimation of compact binaries observed with LISA, *Astron. Astrophys.* **544**, A153 (2012), arXiv:1207.6770 [astro-ph.IM].
- [62] M. Vallisneri, Use and abuse of the Fisher information matrix in the assessment of gravitational-wave parameter-estimation prospects, *Phys. Rev. D* **77**, 042001 (2008), arXiv:gr-qc/0703086.
- [63] S.-J. Huang, Y.-M. Hu, V. Korol, P.-C. Li, Z.-C. Liang, Y. Lu, H.-T. Wang, S. Yu, and J. Mei, Science with the TianQin Observatory: Preliminary results on Galactic double white dwarf binaries, *Phys. Rev. D* **102**, 063021 (2020), arXiv:2005.07889 [astro-ph.HE].
- [64] C. Cutler, Angular resolution of the LISA gravitational wave detector, *Phys. Rev. D* **57**, 7089 (1998), arXiv:gr-qc/9703068.
- [65] B. Ewing, S. Sachdev, S. Borhanian, and B. S. Sathyaprakash, Archival searches for stellar-mass binary black holes in LISA data, *Phys. Rev. D* **103**, 023025 (2021), arXiv:2011.03036 [gr-qc].
- [66] E. M. Gutiérrez, L. Combi, S. C. Noble, M. Campanelli, J. H. Krolik, F. G. L. Armengol, and F. García, Electromagnetic Signatures from Supermassive Binary Black Holes Approaching Merger, *Astrophys. J.* **928**, 137 (2022), arXiv:2112.09773 [astro-ph.HE].
- [67] C. Roedig, J. H. Krolik, and M. Coleman Miller, Observational Signatures of Binary Supermassive Black Holes, *Astrophys. J.* **785**, 115 (2014), arXiv:1402.7098 [astro-ph.HE].
- [68] H. Tagawa, S. S. Kimura, Z. Haiman, R. Perna, and I. Bartos, Observable Signature of Merging Stellar-mass Black Holes in Active Galactic Nuclei, *Astrophys. J.* **950**, 13 (2023), arXiv:2301.07111 [astro-ph.HE].
- [69] I. Bartos, B. Kocsis, Z. Haiman, and S. Márka, Rapid and Bright Stellar-mass Binary Black Hole Mergers in Active Galactic Nuclei, *Astrophys. J.* **835**, 165 (2017), arXiv:1602.03831 [astro-ph.HE].
- [70] K. Schumacher, N. Yunes, and K. Yagi, Gravitational wave polarizations with different propagation speeds, *Phys. Rev. D* **108**, 104038 (2023), arXiv:2308.05589 [gr-qc].
- [71] M. Tinto and S. V. Dhurandhar, Time-delay interferometry, *Living Rev. Rel.* **24**, 1 (2021).